A Model Study of the Air–Sea Interaction Associated with the Climatological Aspects and Interannual Variability of the South Asian Summer Monsoon Development

NGAR-CHEUNG LAU AND MARY JO NATH

NOAA/Geophysical Fluid Dynamics Laboratory, Princeton University, Princeton, New Jersey

(Manuscript received 19 January 2011, in final form 30 June 2011)

ABSTRACT

The climatological characteristics and interannual variations of the development of the South Asian summer monsoon (SASM) in early summer are studied using output from a 200-yr simulation of a coupled atmosphere–ocean general circulation model (CM2.1). Some of the model results are compared with corresponding observations. Climatological charts of the model and observational data at pentadal intervals indicate that both the precipitation and SST signals exhibit a tendency to migrate northward. Enhanced monsoonal precipitation at a given site is accompanied by a reduction in incoming shortwave radiation and intensification of upward latent heat flux, and by oceanic cooling.

An extended empirical orthogonal function analysis is used to identify the dates for initiation of the northward march of SASM in individual summers. It is noted that early monsoon development prevails after the mature phase of La Niña events, whereas delayed development occurs after El Niño.

Sensitivity experiments based on the atmospheric component of CM2.1 indicate that the effects of SST forcings in the tropical Pacific (TPAC) and Indian Ocean (IO) on monsoon development are opposite to each other. During El Niño events, the atmospheric response to remote TPAC forcing tends to suppress or postpone monsoon development over South Asia. Conversely, the warm SST anomalies in IO, which are generated by the ''atmospheric bridge'' mechanism in El Niño episodes, lead to accelerated monsoon development. The net result of these two competing effects is an evolution scenario with a timing that is intermediate between the response to TPAC forcing only and the response to IO forcing only.

1. Introduction

The South Asian summer monsoon (SASM) is one of the most prominent circulation systems in the Northern Hemisphere, and is the subject of numerous investigations (e.g., see reviews by Krishnamurti and Surgi 1987; Webster et al. 1998; Webster 2006; Goswami 2005b; and Ding and Sikka 2006, among others). In most years, the evolution of this phenomenon is characterized by distinct stages of development. The timing and spatial development of SASM in early summer are of particular interest, since this phase heralds the start of the growing season in one of the most densely populated regions of the world and has profound implications on local agriculture and economy. It is well known from analyses of long-term averaged data that the earliest monsoon rains occur over the southeastern Bay of Bengal (BoB) in early May and move progressively northwestward to the Indian Subcontinent (e.g., Wang and Lin 2002). Precipitation signals also advance northeastward from the southern Arabian Sea to the southwestern coast of India. The monsoon rains make landfall over southern India in early June, then march systematically northward, and reach the southern edge of the Tibetan Plateau in late June–early July.

The spatiotemporal behavior of the climatological SASM is evidently linked to the evolution of the principal heat sources and sinks in that region. The seasonal development of these forcings is in turn associated with various types of energy exchanges over land and ocean surfaces (e.g., Webster 1983; Li and Yanai 1996), as well as interactions between the monsoonal circulation and local orographic features (Yanai et al. 1992). Wang and Xu (1997) noted a tendency for tropical intraseasonal oscillations to be phase-locked with the annual cycle. The resulting climatological intraseasonal oscillations are characterized by monsoon features (referred to by these authors as ''singularities'') that occur with marked

Corresponding author address: Ngar-Cheung Lau, NOAA/Geophysical Fluid Dynamics Laboratory, Princeton University, Forrestal Campus, P.O. Box 308, Princeton, NJ 08542.
E-mail: gabriel.lau@noaa.gov

DOI: 10.1175/JCLI-D-11-00035.1

regularity in certain fixed phases of the seasonal calendar. The northward advance of the SASM on intraseasonal time scales could also result from dynamical coupling of the prevalent modes of motion with the large-scale wind shear environment (Jiang et al. 2004), or with wind-induced surface heat fluxes (Bellon and Sobel 2008). Fu et al. (2003) have offered a comprehensive discussion of the causes of northward-propagating monsoon signals over South Asia.

It is well known that the monsoon evolution in individual summers exhibits notable deviations from the climatological scenario portrayed above (e.g., see reviews by Shukla 1987; Webster et al. 1998; and Gadgil et al. 2011). Among the various facets of monsoon development, the interannual variability of the onset date of the SASM has long received attention from both the research and forecasting communities. For instance, Joseph et al. (1994, 2006) have documented the monsoon dates of initiation over southern India from 1870 to near present. Their results show that extreme cases of onset have occurred in as early as the first week of May, and as late as the third week of June.

Many investigations have been launched to study the mechanisms associated with the year-to-year fluctuations of SASM development. Joseph et al. (1994) noted that the monsoon onset is typically delayed in the summer after the mature phase of warm El Niño–Southern Oscillation (ENSO) events. This relationship suggests a possible role of tropical Pacific (TPAC) sea surface temperature (SST) anomalies in modulating SASM evolution. An alternative source of oceanic forcing is the anomalous SST field in the Indian Ocean (IO). The oceanic conditions in IO are known to be influenced by ENSO events (e.g., see Klein et al. 1999; Alexander et al. 2004). Thus it is of considerable interest to assess the relative impacts of remote oceanic changes in TPAC versus the more local SST anomalies in IO. In addition to atmospheric coupling with oceanic sites in various geographical sites, other factors that might affect the timing of monsoon development include land surface conditions and snow cover over nearby regions (e.g., Yang et al. 1996; Robock et al. 2003), the occurrence of intraseasonal oscillations (Goswami 2005a), and prevailing circulation patterns in the extratropics (Chang et al. 2001).

The principal objective of the present study is to further delineate the nature of air–sea interaction accompanying the development of SASM in early summer, in the contexts of both climatological development and interannual variability. This investigation is primarily based on the diagnosis of the output from a multicentury integration of a coupled general circulation model (GCM) at the Geophysical Fluid Dynamics Laboratory (GFDL), as well as from several auxiliary experiments highlighting certain aspects of the air–sea coupling. Whenever feasible, the model findings are compared with corresponding observations. This set of model experiments was previously diagnosed by Lau and Nath (2009, hereafter referred to as LN09), with a focus on the monsoon system over the South China Sea and subtropical western North Pacific (SCS–WNP). In the present study, we shall turn our attention to the processes contributing to the development of the SASM. It should be stressed that the SCS–WNP and South Asian monsoons are embedded in rather distinct large-scale environments. In particular, land–sea contrasts, orographic influences, and oceanic upwelling are much more prominent in South Asia than in the SCS–WNP sector. These factors partially account for substantial differences in the ambient flow structure over these two regions. For instance, the quasi-stationary subtropical anticyclone over the western North Pacific exerts a strong influence on the SCS–WNP monsoon, whereas the prevalent summertime flow pattern over South Asia is dominated by southwesterlies near the surface and a strong easterly jet stream in the upper troposphere. Moreover, the seasonal monsoon march over the two regions exhibits distinct migratory signals, with predominantly northeastward development over SCS–WNP, and northward or northwestward propagation over South Asia. In view of these marked differences between the monsoon systems over SCS–WNP and South Asia, it is worthwhile to examine in more detail the characteristics of SASM by using a new set of diagnostic tools that are particularly suited for studying the monsoon development in that region.

The sources of the model and observational datasets examined in this study are documented in section 2. The atmospheric and oceanic changes accompanying the climatological evolution of SASM are described in section 3. Outstanding cases of early and delayed development are identified in section 4, and their temporal correspondence with the ENSO cycle in the tropical Pacific is explored in section 5. The impacts of ENSO-related SST variations in TPAC and IO on SASM evolution are considered separately in sections 6 and 7, respectively. The net effect of oceanic forcings from these two sectors on SASM is illustrated in section 8. A summary and discussion of the essential findings are offered in section 9.

2. Model and observational datasets

The detailed specifications of the individual datasets for this study have been provided by LN09 (see their section 2). Hence only a brief summary is offered here.

The primary model archive is generated by a 200-yr simulation under constant 1860 radiative forcing with a GFDL coupled atmosphere–ocean model (CM2.1), as documented by Delworth et al. (2006). The atmospheric component (AM2.1) of this model has a latitudinal and

longitudinal resolution of 2° and 2.5°, respectively, and has 24 vertical levels. The numerics and physics of AM2.1 are described by the GFDL Global Atmospheric Model Development Team (2004). The oceanic component [Modular Ocean Model version 4 (MOM4); see documentation by Griffies et al. 2003] has 50 vertical layers and a latitude–longitude resolution of 1° outside the tropics. The meridional resolution increases to 1/3° near the equator.

The observational data resources for this study include reanalysis products of the 40-yr European Centre for Medium-Range Weather Forecasts (ECMWF) Re-Analysis (ERA-40) for the near-surface and 850-mb winds; precipitation data from the Global Precipitation Climatology Project (GPCP); shortwave (SW) radiative fluxes compiled by the International Satellite Cloud Climatology Project; and latent heat (LH) fluxes over oceanic sites produced by the objectively analyzed air–sea fluxes (OAFlux) project. The climatological SST observations for individual calendar days are based on long-term averages of the National Centers for Environmental Prediction–National Center for Atmospheric Research (NCEP–NCAR) reanalyses of skin temperature for the 1968–96 period.

3. Atmospheric and oceanic changes accompanying development of the climatological SASM

To discern the rather rapid variations occurring in the initiation phase of the climatological SASM, ''pentadal tendencies'' of selected fields are computed using the following procedure: the long-term climatology for each 5-day period (pentad) is computed; the pentadal tendency centered at a given pentad P is then calculated by subtracting the value for the preceding pentad (i.e., $P - 1$) from the value for the succeeding pentad ($P + 1$). The distributions are shown of climatological pentadal tendencies of 850-mb vector wind (arrows) and precipitation (shading) (Figs. 1a–d), downward shortwave flux (contours) and SST (shading) (Figs. 1e–h), and upward latent heat flux (contours) and SST (shading) (Figs. 1i–l). The first, second, third, and fourth rows of this figure show tendencies centered at the pentads 11–15 May, 21–25 May, 31 May–4 June, and 10–14 June, respectively. All results are obtained from 200-yr averages of the output from the CM2.1 simulation.

In mid-May, substantial precipitation increases and strengthening of the westerly or southwesterly circulation at 850 mb occur along a broad zone extending northeastward from the eastern African coast to southern BoB (Fig. 1a). In the ensuing pentads (see Figs. 1b–d), this band of rainfall and wind changes migrates continuously northward from its original position at 0°–10°N to beyond 20°N in mid-June. The cyclonic wind pattern poleward of the positive rainfall changes over the northern Arabian Sea and BoB (Figs. 1b–c) reveals considerable intensification of the monsoon troughs in these regions. The precipitation and westerly wind increases over southern India and nearby waters in mid-May (Fig. 1a) are replaced locally by drying and anticyclonic tendencies one month later (Fig. 1d).

The positive rainfall changes during the development of SASM are coincident with increased cloud cover and reduced SW fluxes (see contours in Figs. 1e–h). The increased surface wind speeds associated with the strengthened westerly monsoon flow are accompanied by enhanced latent heat fluxes from the underlying ocean (contours in Figs. 1i–l). The SST tendency field is plotted in Figs. 1e–l using shading. The cooling tendency seen in this pattern is consistent with the decrease in SW flux and increase in LH flux. Because of the thermal inertia of the oceanic mixed layer, the strongest signals in SST tendency typically appear 2–4 pentads after the corresponding signals in SW or LH flux at the same location, with the poleward advancing centers of negative SW flux and positive LH flux tendencies being located to the north of the center of SST cooling.

Another feature of interest in the SST tendency patterns (shading in Figs. 1e–l) is the falling temperatures off eastern Africa starting from the end of May, and along the southeastern coast of the Arabian Peninsula 2–4 pentads later. This development is evidently linked to the upwelling driven by the alongshore component of the local near-surface flow, the influence of which also spreads northward with time (see wind vectors in Figs. 1a–d).

The observational counterpart of Fig. 1, as computed using the datasets listed in section 2, is presented in Fig. 2. The observed precipitation tendency (shading in Figs. 2a–d) exhibits more small-scale features than the corresponding model results. Nonetheless, the tendency for northward migration of the precipitation signal is still discernible over the Arabian Sea and northern BoB. The collocation of increasing precipitation with strengthened 850-mb westerlies or southwesterlies, reduced SW flux, and increased LH flux, as noted in the model patterns, is apparent in the observational charts. The observations are also in support of the near-quadrature spatiotemporal relationship between the simulated tendencies in surface fluxes and SST.

The spatial displacements and temporal lags between the various model and observed fields considered in Figs. 1, 2 are examined in greater detail in Fig. 3, which shows using contours the time–latitude distributions of LH, SW, and SST. The corresponding distributions of the precipitation field are shown throughout using shading. All data presented here are centered pentadal tendencies averaged between 60° and 90°E.

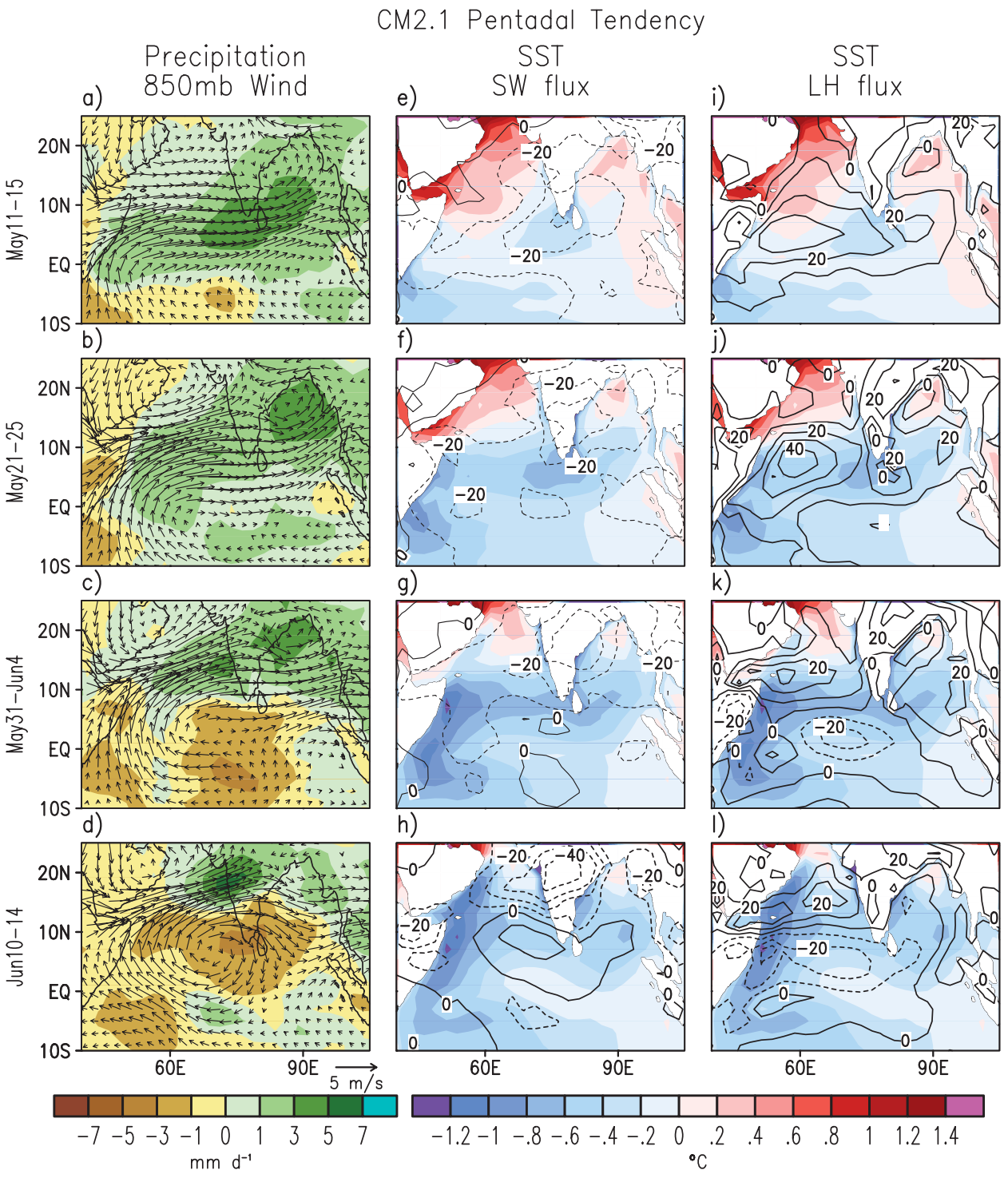

FIG. 1. Distributions of the 200-yr climatology of (a)–(d) precipitation (shading) and 850-mb wind vector (arrows), (e)–(h) SST (shading) and downward SW flux (contours; interval: 10 W m^{-2}), and (i)–(l) SST (shading) and upward LH flux (contours; interval: 10 W m^{-2}). The patterns displayed here are pentadal tendencies (see definition in text) centered on (a),(e),(i) 11–15 May, (b),(f),(j) 21–25 May, (c),(g),(k) 31 May–4 Jun, and (d),(h),(l) 10–14 Jun. All results are based on output from the CM2.1 simulation.

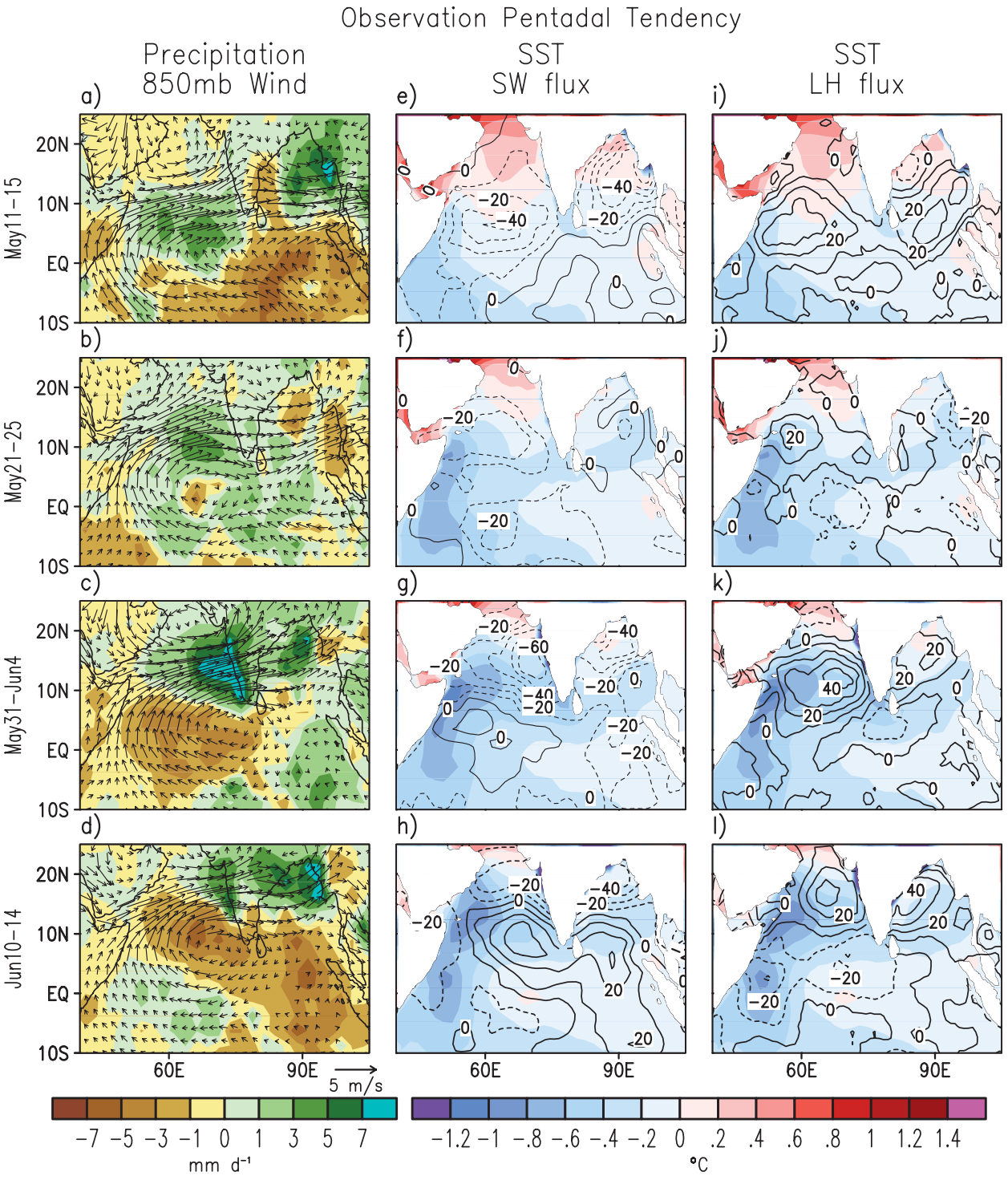

FIG. 2. As in Fig. 1, but for patterns based on long-term averages of various observational datasets.

In the model patterns, the slanting of the axes of extremum in rainfall tendency (shading in Figs. 3a,c,e) clearly indicates the continuous northward advance of the precipitation signal with time. Rainfall increases are seen to coincide with positive changes in LH and negative change in SW (contours in Figs. 3a,c), and vice versa. A well-defined quadrature relationship is evident between the pattern for SST tendency (Fig. 3e) and the

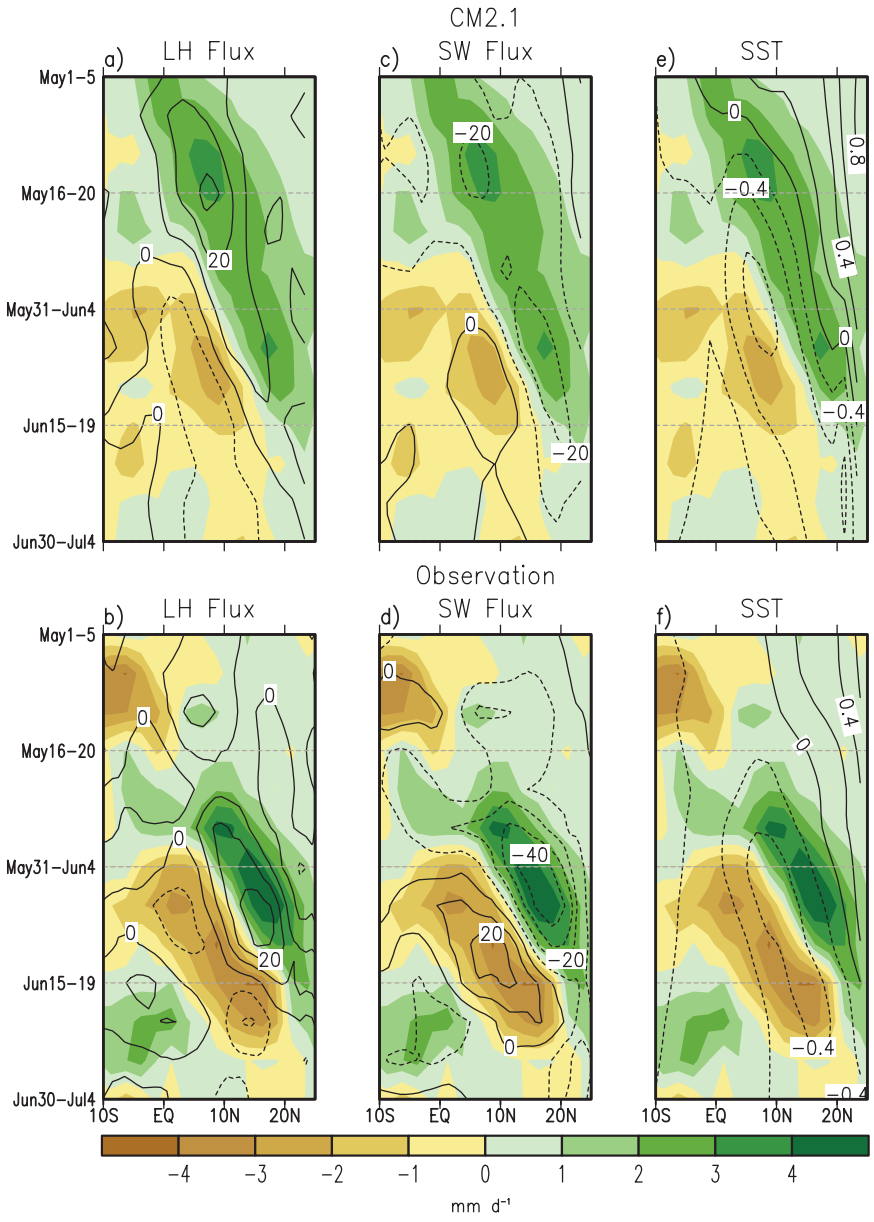

FIG. 3. Contour patterns show variations with latitude (abscissa) and time (ordinate) of climatological (a),(b) LH flux (interval: 10 W m^{-2}), (c),(d) SW flux (interval: 10 W m^{-2}), and (e),(f) SST (interval: 0.2°C). Shading patterns show the corresponding precipitation field. All contour and shading patterns displayed are pentadal tendencies (see definition in text) based on (a),(c),(e) CM2.1 output and (b),(d),(f) observations. The precipitation values are obtained by averaging over all grid points between 60° and 90°E. The LH, SW, and SST values are obtained by averaging only over ocean grid points between 60° and 90°E. All data are plotted at pentadal intervals.

patterns for net surface fluxes (Figs. 3a,c), with negative SST tendencies reaching maximum amplitudes at about three pentads after the occurrence of the largest changes in LH and SW.

The contour and shaded patterns in Fig. 3c indicate that maximum precipitation tendency at a given latitude leads the strongest SST cooling at the same latitude by 3–4 pentads. In a given pentad, the strongest SST cooling occurs at about 10° of latitude to the south of the maximum in precipitation tendency. This development of an SST gradient underneath the zone of maximum precipitation tendency, with decreasing temperatures to the

south and relatively warmer temperatures to the north, contributes to the continued northward migration of the precipitation signal.

The model results (Figs. 3a,c,e) are generally supported by the observational data (Figs. 3b,d,f). The amplitudes of the observed precipitation and flux tendencies are higher than the simulated values. The major model signals make an earlier appearance in the seasonal calendar (typically by 2–3 pentads) than the corresponding observational results.

The spatiotemporal relationships among the changes in precipitation, SST, and SW and LH fluxes during SASM development, as delineated in Figs. 1–3, are in accord with the findings reported by Fu et al. (2003) on the basis of another coupled model, and by Sengupta and Ravichandran (2001) and Sengupta et al. (2001) using buoy measurements in BoB and satellite data. By comparing simulations based on air–sea coupled models with output from stand-alone atmospheric models with prescribed SST forcings, Rajendran and Kitoh (2006) and Pegion and Kirtman (2008) demonstrated that the phase relationships between intraseasonal variations of precipitation, surface flux, and SST fields are much improved or notably stronger in the presence of coupling. The analysis by Fu et al. (2007) of model experiments with and without air–sea coupling further confirms that the predictability of intraseasonal oscillations in the Asian–western Pacific region is noticeably enhanced when air–sea interaction is incorporated. The cumulative evidence from the above studies is in strong support of the important role of air–sea coupling in the monsoon variability on intraseasonal time scales.

Fu et al. (2003, see their section 4b) further noted that the preferred northward migration of the monsoon signals over South Asia may partially be attributed to strong north–south asymmetries in the climatological low-level wind and cloud cover over that region. During the boreal summer, the mean surface southwesterlies and southeasterlies prevail in the northern and southern IO, respectively, and the mean cloud amount over IO is much larger north of 10°S than south of that latitude. Superposition of wind and cloud perturbations driven by monsoonal convection on these asymmetric mean states would result in different changes in LH and SW fluxes (and hence SST) at locations situated north and south of the convection zone. The results presented by Fu et al. indicate that the meridional pattern of such SST changes is conducive to the northward migration of the convection.

4. Identification of episodes of early and late SASM development

To identify outstanding cases with large deviations from the climatological norm, we have applied an extended empirical orthogonal function (EEOF) analysis (see Weare and Nasstrom 1982 for details) to the pentadal precipitation tendencies for the nine pentads from 1–5 May to 10–14 June in individual years. For both model and observational data, the analysis is conducted on a lag-correlation matrix with a total of eight lags. The individual elements of this matrix are computed using deviations of the standardized precipitation tendencies in individual pentads of a given year from the average over all pentads within the period from 1–5 May to 10–14 June of the same year. The domain of this EEOF analysis extends from 10°S to 25°N, and 50°E to 100°E. The characteristics of each EEOF mode can be described using a sequence of eight *spatial patterns*, which illustrate the evolution of the precipitation signals at successive time lags. The strength and polarity of each mode during various pentads of different years can be inferred from the time series of *temporal coefficients* associated with that mode.

The first two leading EEOF modes (hereafter referred as EEOF1 and EEOF2) for the CM2.1 data are very similar to each other, except for a quadrature phase shift in space and time. Hence they depict essentially the same phenomenon with a distinct propagating tendency. This pair of modes together explains 7.1% of the total variance. The same remarks apply to EEOF1 and EEOF2 based on GPCP data, which jointly explain 14.6% of the total variance. The small percentages explained by EEOF1 and EEOF2 illustrate that the spatiotemporal fluctuations of precipitation in the SASM region are rather complex, and that such changes on myriad interannual and intraseasonal time scales could be linked to a large variety of characteristic patterns. We shall henceforth confine our attention to the properties of EEOF1 computed using model and observational data. As will be demonstrated in the following analyses, this mode is closely related to the interannual variability of the SASM development in early summer.

The space–time development of the precipitation changes associated with EEOF1 may be illustrated using regression patterns of the local precipitation tendency data versus the standardized temporal coefficients of that mode at various lags. These charts are displayed in Figs. 4a–d for CM2.1 output and Figs. 4e–h for GPCP data. Results for local precipitation tendencies lagging the EEOF1 coefficients by 0, 2, 4, and 6 pentads are shown. For the sake of brevity, the patterns corresponding to lags of 1, 3, 5, and 7 pentads are not presented. It is seen that EEOF1 in the model and observed atmospheres share many common characteristics. Strong precipitation tendencies first appear near a zonally elongated belt over the equatorial IO (Figs. 4a,e). This feature moves systematically northward with time, and arrives at the northern portion of the Arabian Sea, Indian Subcontinent, and BoB about 4 pentads later (Figs. 4c,g), at which time a new center of

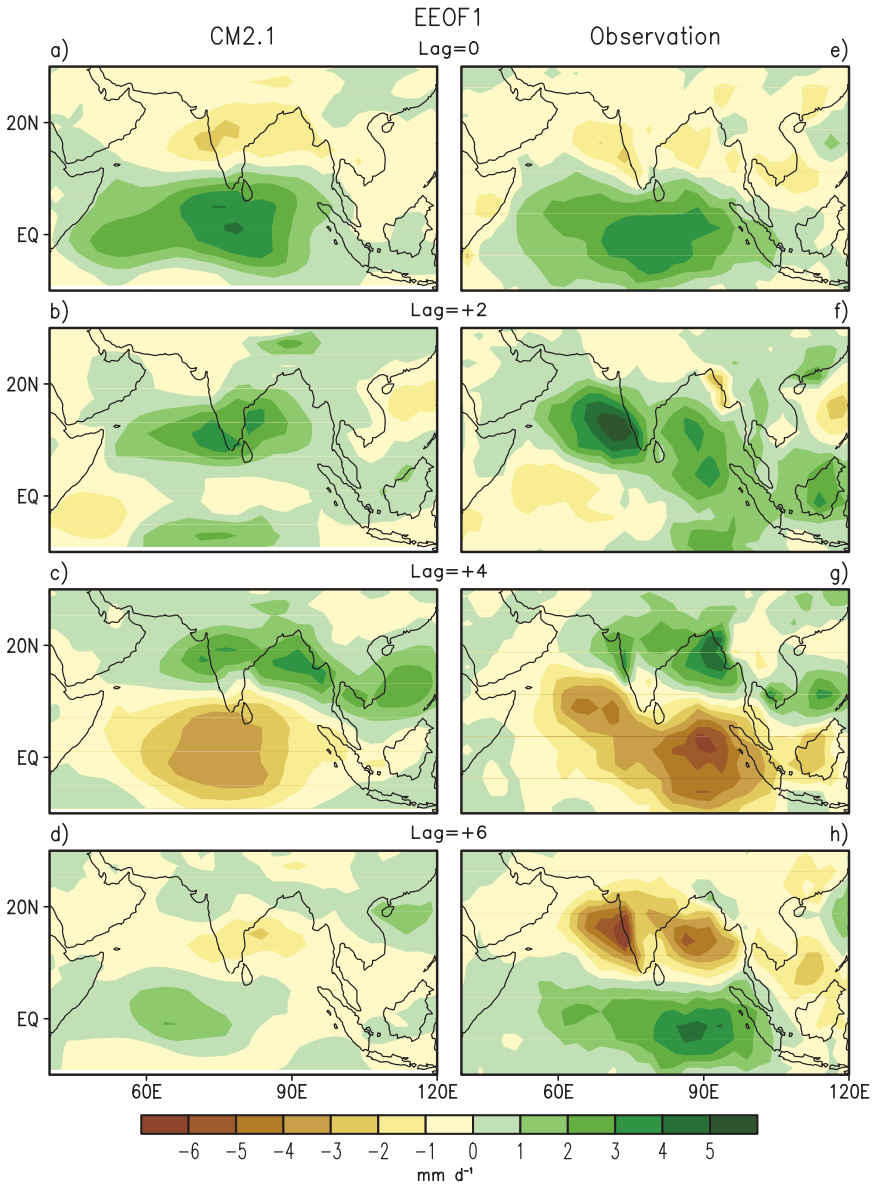

FIG. 4. Regression charts of pentadal precipitation tendency data at individual grid points vs the temporal coefficients of EEOF1, at a temporal lag of (a),(e) 0, (b),(f) 2, (c),(g) 4, and (d),(h) 6 pentads. Results are shown for (a)–(d) CM2.1 output and (e)–(h) GPCP data. EEOF analysis of the model (observational) data is based on a staggered grid of 170 (140) points, with latitude–longitude spacings of 2° × 5° (2.5° × 5°).

the opposite polarity is initiated near the equator. The latter signal also exhibits a tendency to migrate northward (Figs. 4d,h). This sequence of precipitation changes is similar to that reported by Kang et al. (1999, see their Fig. 11) based on an EEOF analysis of the climatological intraseasonal component of high-cloud observations over South and East Asia. The precipitation patterns in Figs. 4c,g are also reminiscent of that associated with the wet phase of Cycle II of the observed climatological intraseasonal oscillations, as documented by Wang and Xu (1997, see their Fig. 12a).

The time series of the climatological average of the EEOF1 coefficients for individual pentads in the seasonal calendar are shown by the orange curves in Figs. 5a,b for CM2.1 and observational data, respectively. For the model atmosphere, this time series exhibits a positive peak on 16–20 May. The timing of this peak (hereafter referred to as the "climatological peak") implies that the long-term

averaged monsoon development begins with the appearance on 16–20 May of the regression pattern at zero-lag (i.e., Fig. 4a). The subsequent evolution is portrayed by patterns in Figs. 4b,c,d, at 2, 4, and 6 pentads after 16–20 May, respectively. In particular, the arrival of the precipitation over southern India (which corresponds to the conventional "monsoon onset" in this region) is best matched with the regression pattern at a lag of 2 pentads (i.e., Fig. 4b), thus implying that the averaged onset occurs on about 26–30 May. This inferred timing of the climatological SASM development is consistent with the findings based on the long-term averaged charts in Fig. 1. By the same token, inspection of the results for the observed atmosphere (Figs. 2, 4e–h, 5b) reveals that the observed EEOF1 coefficients reach a climatological peak on 21–25 May, and that the monsoon onset typically takes place on about 31 May–4 June.

As an independent check of the relevance of our EEOF analysis to the development of SASM, we have considered two other objective indicators of monsoon onset. Goswami and Xavier (2005) examined the tropospheric temperature (TT) within the layer between 700 and 200 mb, and noted that the monsoon onset over South Asia coincides with the reversal of the meridional gradient of TT (hereafter referred to as ΔTT). These investigators estimated ΔTT by subtracting the average of TT over the 10°–35°N, 30°–110°E box from the corresponding quantity over the 15°S–10°N, 30°–110°E box. Wang et al. (2009) proposed an alternative "onset circulation index" (OCI) based on the average of the zonal wind at 850 mb over the 5°–15°N, 40°–80°E box, and demonstrated that SASM onsets typically occur when this index crosses the threshold of about 6 m s^{-1}. The time series of the ΔTT and OCI indices (see green solid and dashed curves, respectively), as computed using the above procedures for both CM2.1 and observational data, are overlaid on the time series of EEOF1 coefficients in Fig. 5. It is seen that the dates when ΔTT changes from negative to positive are very close to those when OCI exceeds 6 m s^{-1}, and that these dates match well with the onset dates as inferred from the EEOF1 coefficients (i.e., about 2 pentads after the climatological peaks of EEOF1 coefficients; see arguments in the preceding paragraph). This consistency between the results based on EEOF1 coefficients and the ΔTT or OCI indices illustrates the reliability of the EEOF tools for identifying SASM onsets.

We wish to emphasize here that EEOF1 serves not only as an index for inferring the arrival of precipitation over South Asia (i.e., timing of the conventional monsoon onset, as seen in Figs. 4b,f), but also as a descriptor of the intensity of the precursory signal over IO before the onset (Figs. 4a,e) and the subsequent northward migration of these signals (Figs. 4c,d,g,h). Specifically, if the time series

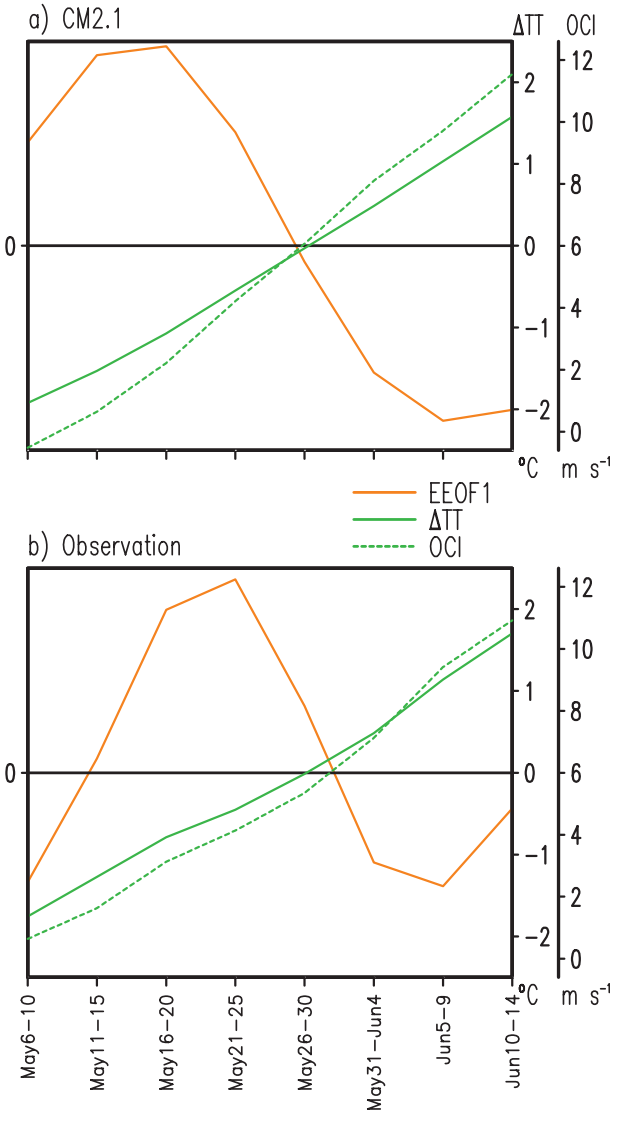

FIG. 5. Time series of the climatological temporal coefficients of EEOF1 (orange curve; in arbitrary units), meridional gradient of tropospheric temperature over South Asia (ΔTT; solid green curve), and OCI (dashed green curve), as computed using multi-year averages of (a) CM2.1 data and (b) observations at individual pentads. Note different scales for the ΔTT and OCI indices shown on the right ordinate axis.

of EEOF1 temporal coefficients for a certain summer exhibits a positive peak in a period earlier (later) than the corresponding climatological peak, *both* the SASM onset *and* the poleward evolution of the monsoonal precipitation before and after the onset in that particular year would occur earlier (later) than normal. We shall henceforth use the terms "monsoon development" or "monsoon evolution" to refer to the entire sequence of precipitation changes as represented by the EEOF patterns in Fig. 4 over a time span of about 6 pentads. These

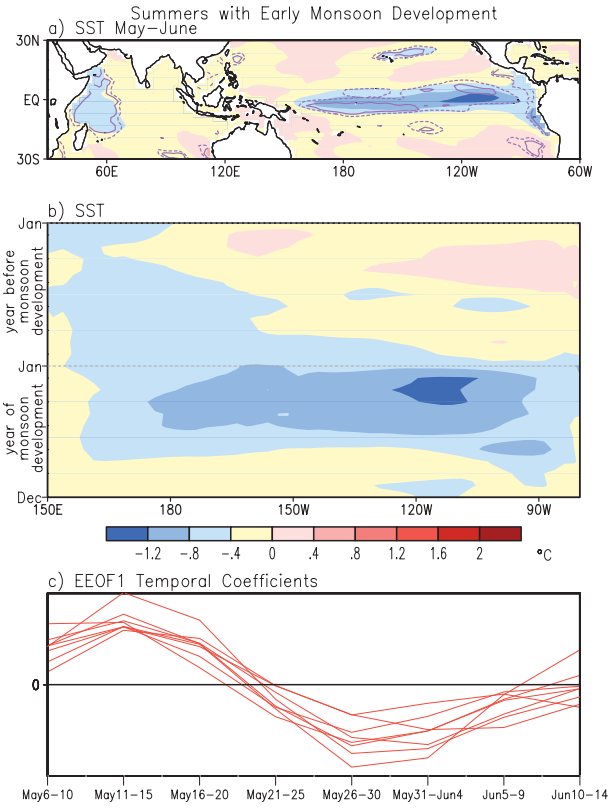

FIG. 6. (a) Distribution of the composite pattern of the anomalous SST field in the May–June period for summers with early SASM development. Purple solid (dashed) contours indicate anomalies exceeding the 95% (90%) significance level. (b) Variations with longitude (abscissa) and time (ordinate) of the composite monthly mean SST anomalies for summers with early SASM development. Values are based on averages between 5°S and 5°N. (c) Time series of the temporal coefficients of EEOF1 for the eight summers with early SASM development, which are selected for constructing the composites in (a),(b). See text for criteria for identifying these summers with early development. All results are based on output from the CM2.1 simulation.

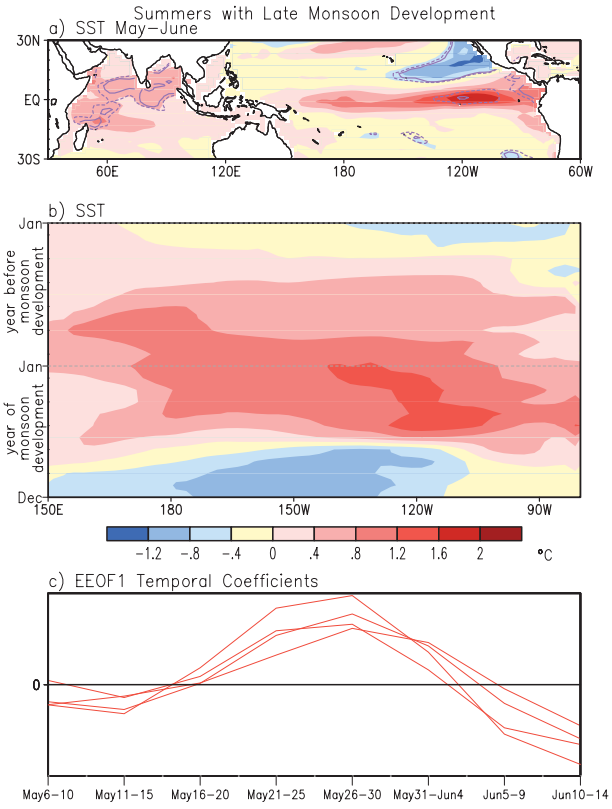

FIG. 7. As in Fig. 6, but for composites over four selected summers with late SASM development. (c) Time series of the temporal coefficients of EEOF1 for these summers.

terms are to be distinguished from the conventional reference to abrupt monsoon onsets, which take place on much shorter time scales.

Years with early development are selected by requiring that the time series of EEOF1 temporal coefficients for these years exhibit a positive maximum in the 11–15 May pentad (i.e., one pentad ahead of the climatological peak), and that the values of these maxima lie within the 80–100th percentile of all maxima that appear on 11–15 May. These criteria are satisfied by eight summers in the 200-yr model dataset. The temporal variations of the EEOF1 coefficients for these selected summers (hereafter referred to as summers with early monsoon development) are shown in Fig. 6c. Analogously, years with delayed development are those with EEOF1 temporal coefficients peaking at the 26–30 May pentad, which is two pentads later than the climatological peak, and with maxima exceeding the 80th percentile threshold of all maximum values occurring on 26–30 May. The time series of the four summers with late monsoon development that meet these requirements are displayed in Fig. 7c. As noted in the earlier part of this section, the largest increases of the monsoon rain over the southern half of India occur at two pentads after the maximum in EEOF1 coefficients is reached (see Fig. 4b). Hence the summers with early and late development actually correspond to the arrival of the monsoon at the southern half of India on about 21–25 May and 5–9 June, respectively.

5. Association of interannual variability of SASM development with ENSO

The typical oceanic surface conditions in summers with early and late monsoon development are illustrated using composite charts of the SST anomaly field, shown in Figs. 6a, 7a. These patterns portray the SST conditions for the months of May and June in the year of occurrence of the early or late development (hereafter referred to as monsoon development year). Figures 6b, 7b

show the variation with time and longitude of the meridional average of the monthly mean SST anomaly over the band between 5°S and 5°N. The time (ordinate) axis in Figs. 6b, 7b extends over the 24-month period from January of the year prior to the monsoon development year to December of the monsoon development year.

The contrast between the SST anomalies during summers with early and late development is clearly evident from the results in Figs. 6, 7. Early SASM development is coincident with cold SST anomalies along the equatorial Pacific. The overall pattern in Fig. 6a bears a considerable resemblance to observed La Niña conditions (e.g., Larkin and Harrison 2002). The temporal development in Fig. 6b indicates that early development occurs a few months after the cool SST anomaly in the TPAC has attained maturity in February–April of the same year. On the contrary, delayed monsoon development is accompanied by an SST pattern in the TPAC (Fig. 7a) that is similar to El Niño events in the CM2.1 simulation (Kug et al. 2010), with the largest positive SST anomalies appearing in the first half of the monsoon development year, followed by a transition to below-normal SST conditions in the second half (Fig. 7b).

In view of the small number of samples (four cases) used in constructing the composites for summers with late monsoon development (Fig. 7), the robustness of signals presented in that figure is further tested by considering summers with EEOF1 temporal coefficients reaching maxima on 31 May–4 June (i.e., one pentad later than that examined in Fig. 7) and with magnitudes lying above the 80th percentile. This criterion is satisfied by three summers in the CM2.1 simulation. Composites of the SST anomalies based on this set of summers (not shown) are similar to, and have higher amplitudes than, their counterparts in Figs. 7a,b.

The notable relationships between timing of the SASM evolution and ENSO-related SST variability are further scrutinized by composite analysis of El Niño and La Niña events simulated by CM2.1. ENSO episodes correspond to those time periods in which the smoothed monthly SST anomalies in the equatorial central Pacific stay above 0.4°C or below −0.4°C for six consecutive months or longer. Altogether, 34 El Niño and 45 La Niña events are identified using this method. Further details of this selection procedure are given in LN09 (see their section 5). The time series of EEOF1 temporal coefficients over these sets of El Niño events (La Niña) are displayed in Fig. 8a using red (blue) curves. All composites are performed over the temporal coefficients for the year after the initiation year of each ENSO event [i.e., year (1) based on the nomenclature of LN09].

Figure 8a clearly indicates a significant phase shift of 2–3 pentads between the typical monsoon development in El Niño and La Niña episodes. The composite time series for cold events (blue curve) peaks in the 11–15 May pentad, which implies earlier monsoon development than normal, since the climatological peak for EEOF1 coefficients occurs on 16–20 May (see Fig. 5a). In contrast, warm episodes (red curve) attain maximum values on 21–30 May, thus indicating delayed monsoon development. These inferences based on EEOF1 coefficients are supported by the time series of the composites of ΔTT and OCI (see definition in section 4) over the El Niño and La Niña events in the CM2.1 simulation, shown in Fig. 8d. The latter independent indices also show that the monsoon onset in El Niño (La Niña) episodes takes place later (earlier) than normal.

As a check of the simulated relationship between the timing of SASM evolution and ENSO, the variations of temporal coefficients of EEOF1, as computed using GPCP data (see Figs. 4e–h), are shown in Fig. 8c for four selected summers in the observational record. Two of these summers, 1983 and 1998, correspond to year (1) of the most prominent El Niño episodes in the period covered by the GPCP dataset, whereas the summers of 1989 and 2001 are strong and moderate La Niña events, respectively. The results in Fig. 8c clearly indicate that the peaks of EEOF1 coefficients for cold events (blue curves) lead those for warm events (red curves) by 3–4 pentads.

The timing of the monsoon evolution during each of the selected events in Fig. 8c, as inferred from the EEOF analysis, may be compared with the onset dates over southwestern India as determined by various methods used in the observational literature (e.g., see Table 1 of Joseph et al. 2006 and Fig. 4 of Wang et al. 2009). These observational studies report that the monsoon onsets in 1983 and 1998 are delayed by 10–14 and 0–5 days, respectively, whereas the onset of the 2001 La Niña occurs 7–9 days earlier than normal. These estimates of the onset dates are qualitatively consistent with the EEOF coefficients displayed in Fig. 8c. For the summer of 1989, Wang et al. (2009) noted large discrepancies among onset dates based on different methods. Their estimate deduced from low-level zonal wind data indicates that the onset date in 1989 is about 10 days earlier than normal (also see discussion of Fig. 8f in the following paragraph), and is in support of the corresponding result presented in Fig. 8c.

An additional evaluation of the timing of the observed monsoon development during the years selected in Fig. 8c is performed by inspecting the time series of the observed ΔTT and OCI indices for the same years, shown in Fig. 8f. The latter results are in support of the inferences drawn from the EEOF1 coefficients shown in Fig. 8c, with earlier monsoon onsets during the 1989 and 2001 La Niña episodes, and delayed onsets in the 1983 and 1998 El Niño events.

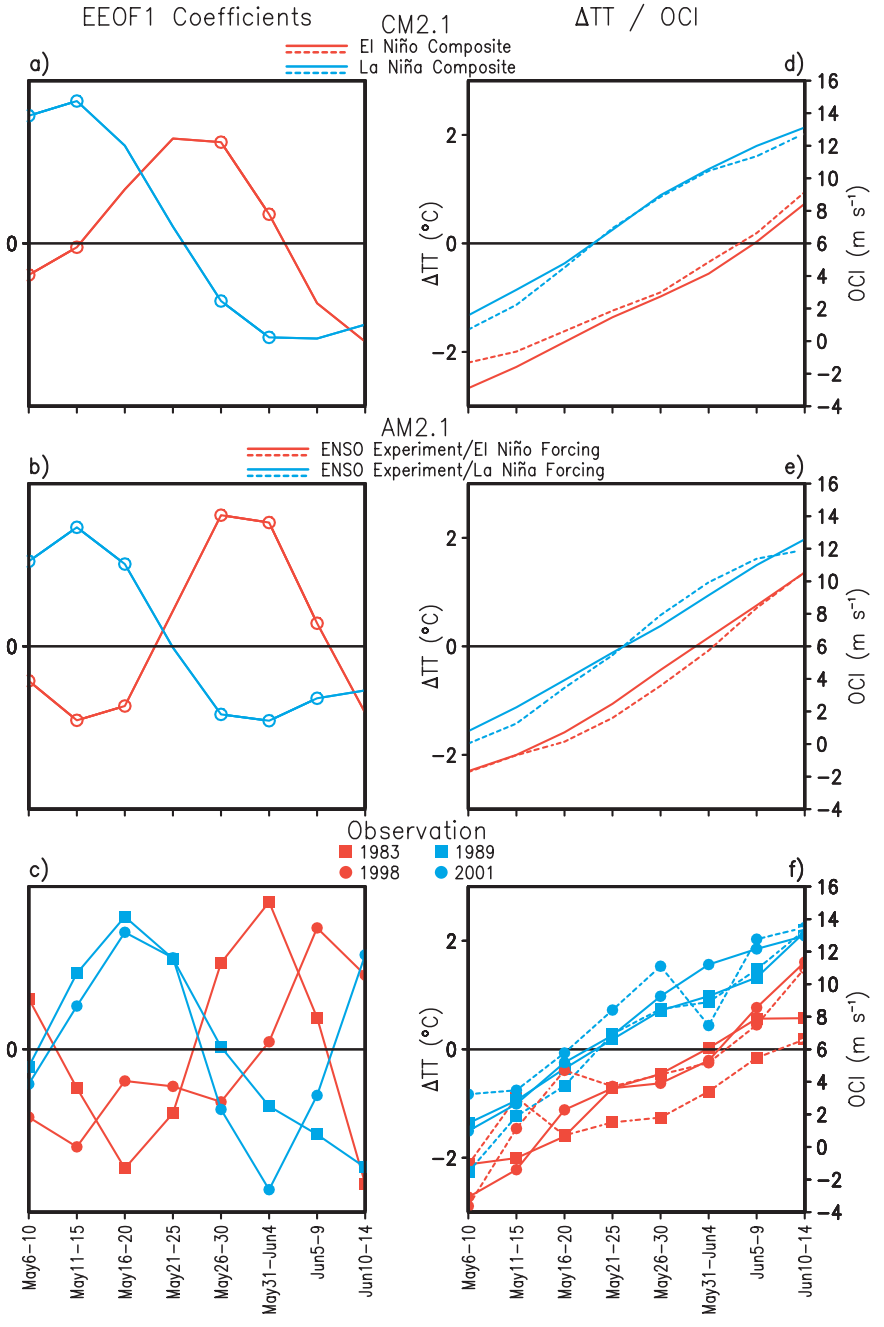

FIG. 8. Time series of (a)–(c) temporal coefficients of EEOF1 (in arbitrary units) and (d)–(f) meridional gradient of tropospheric temperature over South Asia (ΔTT; solid curves) and OCI (dashed curves). Results are based on (a),(d) composites over 34 El Niño events (red curves) and 45 La Niña events (blue curves) appearing in the CM2.1 simulation, (b),(e) averages over 30 independent runs of the ENSO experiment subjected to composite El Niño forcing (red curves) and composite La Niña forcing (blue curves) in TPAC, and (c),(f) selected El Niño (1983, 1998; red curves) and La Niña (1989, 2001; blue curves) events in the observational record. Scales for the ΔTT (OCI) indices are shown in the left (right) ordinate axes of (d)–(f). Open circles in (a),(b) indicate those pentads in which the differences between the values on the red and blue curves exceed the 95% significance level, as estimated by a two-tailed Student's *t* test.

It is evident from the pattern in Fig. 7a that the warm SST anomalies accompanying delayed SASM development are not confined to TPAC, but are also noticeable throughout much of the IO Basin. We proceed to explore the individual impacts of SST forcings in these two regions on monsoon development. The atmospheric component of CM2.1 (referred to as AM2.1) is subjected to time-varying SST forcing prescribed separately in the following two regions:

- the TPAC between 15°S and 15°N, and between 135°E and the American coast, hereafter referred to as the ENSO experiment
- the IO north of 30°S, hereafter referred to as the IO experiment

In each of these experiments, the SST changes in the prescription domain are obtained by separately compositing over the 34 El Niño events or the 45 La Niña events in the CM2.1 simulation. The seasonal SST climatology is imposed at all ocean grid points situated outside of the anomalous forcing domain. Altogether, 30 such integrations, with each being initiated from independent atmospheric conditions, are performed separately for El Niño or La Niña SST composites in a given prescription region. An additional 30-yr climatological experiment (labeled the CLIMO run) is also completed with the model atmosphere being subjected to climatological SST conditions at all ocean grid points. Further details are provided in LN09 (see their section 6a).

6. Responses of SASM development to SST forcing in TPAC

An EEOF analysis is performed on the precipitation tendency data generated in the ENSO experiment. The procedure of this analysis is similar to that described in section 4. In the present application, the input data consist of pentadal averages for the period from 1–5 May to 10–14 June in year (1) of each of the 30 individual runs in the ENSO experiment. The EEOF analysis is conducted separately for responses of the AM2.1 model to El Niño and La Niña composite forcings. For a given polarity of ENSO forcing, the leading pair of modes is in quadrature with each other, and their spatial patterns bear a strong resemblance to those produced in the CM2.1 simulation (see Figs. 4a–d). This finding indicates that, analogous to the interpretation of the CM2.1 data, the EEOF1 and EEOF2 modes based on the ENSO experiment are associated with monsoon development in the SASM sector.

The typical timing of SASM development in the ENSO experiment subjected to El Niño or La Niña forcing may be inferred from the time series of the 30-run average of the temporal coefficients for EEOF1 of the pertinent experiment, shown in Fig. 8b. This result illustrates that the ensemble-mean response of AM2.1 to composite TPAC SST changes in El Niño (La Niña) events is characterized by delayed (accelerated) development. The time series of the ΔTT and OCI onset indices, as computed using the 30-run mean of the output from the ENSO experiment subjected to El Niño (La Niña) forcing, are shown in Fig. 8e using red (blue) curves. These results also indicate late (early) onsets during El Niño (La Niña) events, and thus offer independent support of the inferences drawn from the EEOF1 coefficients.

The impact of El Niño–related SST anomalies in TPAC on the circulation and precipitation fields over the IO Basin is illustrated in greater detail in Figs. 9a–d. This figure shows consecutive 10-day averages of precipitation (shading) and 200-mb velocity potential χ (contours) and divergent wind vector (arrows) for the period from 21–30 April to 21–30 May of year (1). All fields displayed here are obtained by subtracting the 30-yr averages for the CLIMO run from the 30-run averages of the ENSO experiment subjected to El Niño composite forcing.

Figures 9a–d indicate that the primary response of the model atmosphere to El Niño forcing in TPAC is dominated by the migration of a dry zone in the IO sector. This zone is collocated with a maximum in χ, which corresponds to large-scale convergence at 200 mb and subsidence in the midtroposphere. These features are associated with the western sinking branch of the anomalous Walker Circulation forced by warm SST conditions in TPAC. In late April, this dry zone is situated near the eastern edge of the plotting domain (Fig. 9a). In the month of May (Figs. 9b–d), it undergoes a systematic northwestward displacement, and reaches the Indian Subcontinent on 21–30 May.

The northwestward trajectory of the principal anomaly centers in the precipitation and χ fields, as simulated in the ENSO experiment, is very similar to that of the observed outgoing longwave radiation signals (which serve as an indicator of tropical convection) prior to monsoon development over southwestern India (see Fig. 5 of Joseph et al. 1994 and Fig. 6 of Wang et al. 2009). Joseph et al. (1994) have referred to such observed precipitation centers as the equatorial convective cloudiness maximum (ECCM). The evidence presented in Figs. 9a–d indicates that the SST forcing in TPAC could influence the timing of SASM through modulation of the ECCM development over the IO.

The above cumulative results indicate that, in El Niño episodes, the subsidence and dry anomaly forced by warm SST conditions in TPAC migrate toward the central equatorial IO during May of year (1) (Figs. 9b–d). This anomalous development coincides (in both space and time) with the climatological evolution of SASM (Fig. 1). The remote SST forcing in TPAC acts to suppress the

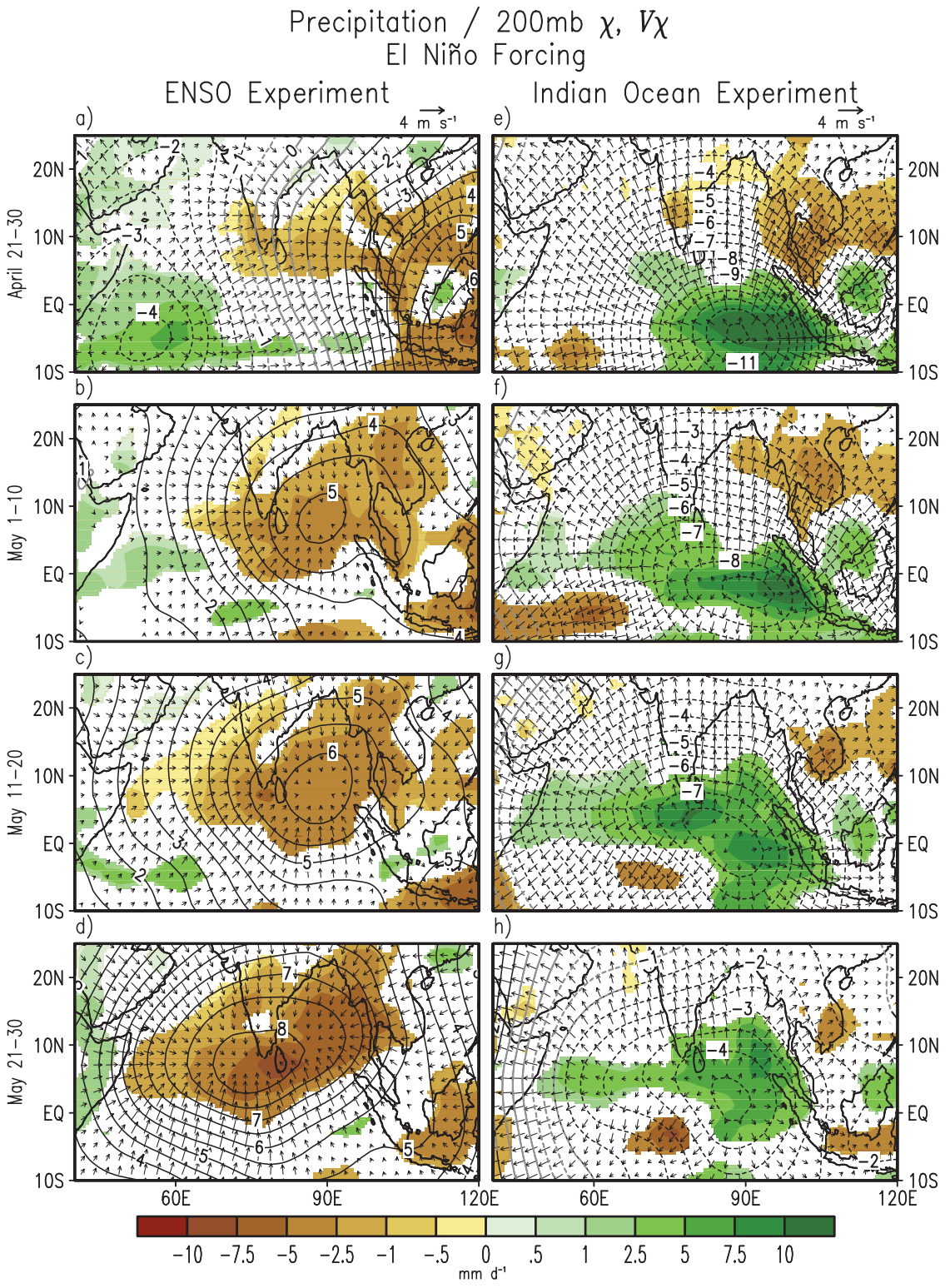

FIG. 9. Distributions of the precipitation (shading) and 200-mb velocity potential (contours; interval: 0.5×10^6 m^2 s^{-1}) and divergent wind component (arrows) for the 10-day periods in (a),(e) 21–30 Apr, (b),(f) 1–10 May, (c),(g) 11–20 May, and (d),(h) 21–30 May of year (1). All results are obtained by subtracting the 30-yr climatology of the CLIMO experiment from the 30-run average of the (a)–(d) ENSO experiment and (e)–(h) IO experiment subjected to composite El Niño SST forcing. Only those precipitation anomalies exceeding the 90% significance level are shown. Velocity potential signals above (below) the 95% significance level are depicted using black (gray) contours.

convective activity over the tropical IO in the initiation phase of SASM. Establishment of such dry ''preconditions'' in May is conducive to weakening or postponement of the northward advance of monsoon rains over South Asia in the pentads that follow.

7. Impacts of air–sea interactions over IO on SASM development

Investigations based on observational analyses and model experimentation (e.g., Klein et al. 1999; Lau and Nath 2003; Xie et al. 2009) demonstrate that ENSO-related SST anomalies in TPAC lead to atmospheric changes in the IO sector, and that the ensuing air–sea interaction over IO in turn alters the SST conditions at these remote sites. The applicability of this ''atmospheric bridge'' concept to the IO warming during El Niño events (see Fig. 7a) has been demonstrated by LN09. In that study, evidence has been presented linking the sinking branch of an anomalous Walker Cell over South Asia to El Niño forcing in TPAC (see Fig. 8a of LN09). This response is accompanied by weakened southwesterly monsoon flow and suppressed precipitation over the Arabian Sea and BoB (see Fig. 8b of LN09). The implied increase in SW flux and decrease in LH flux over these areas (not shown) are in turn associated with SST warming (see Fig. 8a of LN09).

We proceed to consider the feedback effects of the El Niño–induced warming in the IO Basin on the local atmospheric circulation, and the implications of such feedbacks on SASM development. The atmospheric response to the warm SST anomalies in the IO sector during El Niño events may be studied using output from the IO experiment (see end of section 5 for description of the experimental design). The anomalous patterns of precipitation and 200-mb χ and divergent wind for consecutive 10-day periods starting from 21–30 April of year (1), as obtained by subtracting the data for the CLIMO experiment from those for the IO experiment, are displayed in Figs. 9e–h. The plotting format of these panels is identical to that used for showing the responses in the ENSO experiment (Figs. 9a–d).

The most notable feature in the response patterns in Figs. 9e–h is the center of enhanced precipitation and 200-mb divergence, which is situated over the eastern IO just south of the equator in late April (Fig. 9e). These precipitation and circulation responses migrate gradually northward and westward, with influences reaching BoB, southern India, and western IO by the end of May. The path of this migration is similar to the trajectory of the signals generated in the ENSO experiment (see Figs. 9a–d). The model responses in both the ENSO and IO experiments are reminiscent of the propagation characteristics of the observed ECCM over the IO prior to SASM onset, as documented by Joseph et al. (1994) and Wang et al. (2009). The precipitation response generated in the IO experiment in middle and late May of year (1) (Figs. 9g,h) resembles the prevalent rainfall tendency pattern associated with the climatological evolution of SASM in the same phase of the seasonal calendar (Figs. 1a,b). It may hence be inferred from these considerations that the warm SST changes in IO set up a favorable atmospheric environment for reinforcing the development of SASM during its initiation stage.

8. Net effect of SST forcings from TPAC and IO on SASM development

It is apparent from the patterns in Fig. 9 that the atmospheric response to remote El Niño–related oceanic forcing in TPAC (Figs. 9a–d) tends to oppose the response to local SST anomalies in IO induced by the atmospheric bridge mechanism (Figs. 9e–h). The implications of these contrasting responses on SASM development are illustrated in Fig. 10. The contour patterns in this figure depict the variations of the pentadal tendency (see definition at the beginning of section 3) of precipitation as a function of time (ordinate) and latitude (abscissa). These plots are based on averages over the 30 samples of the ENSO experiment (Fig. 10a) and IO experiment (Fig. 10b) subjected to composite El Niño SST forcing. The corresponding distribution based on a composite of the CM2.1 precipitation data over the 34 El Niño events appearing in that simulation is superposed in Fig. 10 using color shading.

The contour patterns in both Figs. 10a,b indicate a northward advance of the precipitation changes with time. However, the monsoon development in the ENSO experiment lags behind that in the IO experiment by approximately three pentads. For instance, maximum positive precipitation tendency is simulated at 10°N (latitude of southern India) in the IO experiment on about 16–20 May (Fig. 10b), whereas the corresponding signal in the ENSO experiment does not reach the same latitude zone until 31 May–4 June (Fig. 10a). This temporal lag between the monsoon evolution in response to SST forcings prescribed in TPAC and IO is in accord with the results in Fig. 9 and the pertinent discussions. Specifically, monsoon development is postponed in the ENSO experiment because of the subsidence and dryness over the region of origination of SASM in middle and late May (Figs. 9c,d), whereas the large-scale ascent and enhanced precipitation over the same site in response to IO warming (Figs. 9g,h) tend to accelerate the monsoon development.

It is of interest to compare the monsoon evolution in the ENSO and IO experiments (contour patterns in Fig. 10) with that simulated in CM2.1 (shading in Fig. 10). The

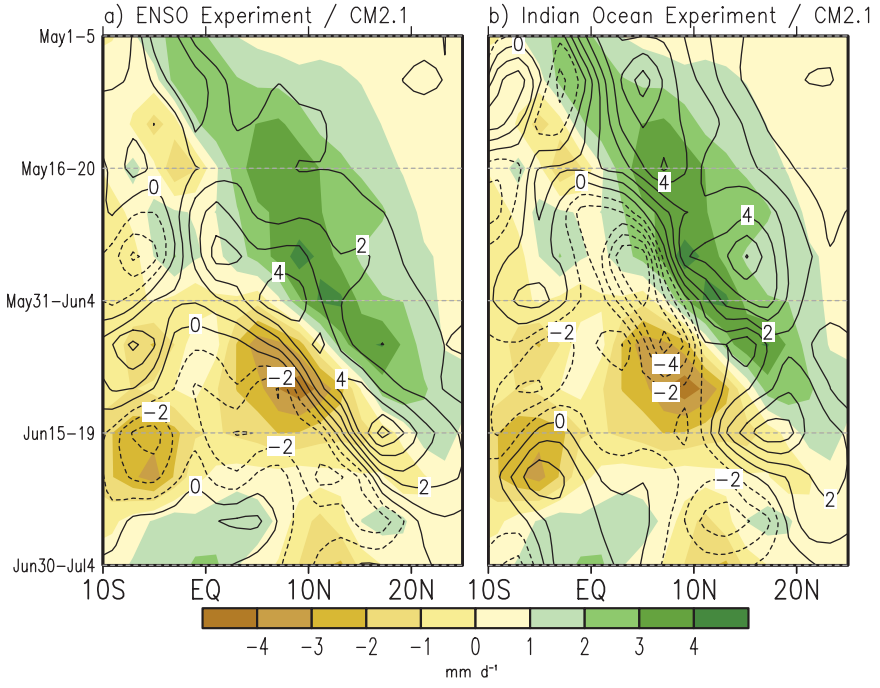

FIG. 10. Contour patterns (interval: 1 mm day^{-1}) show variations with latitude (abscissa) and time (ordinate) of pentadal precipitation tendencies (see text for definition) for 30-run average of data in year (1) of the (a) ENSO experiment and (b) IO experiment, both being subjected to composite El Niño forcing. The corresponding pattern based on composite over data in year (1) of 34 El Niño events appearing in the CM2.1 simulation is superposed using shading. All results are obtained by averaging over the 60°–90°E band.

coupled framework of CM2.1 takes into account the effects of air–sea interaction throughout the world's oceans, which include remote forcing of the atmosphere over IO by SST anomalies in TPAC, SST changes in IO generated by the atmospheric bridge mechanism, and feedbacks of the SST variations in IO on the local atmosphere. The El Niño composite based on output from CM2.1 may hence be viewed as the net result of all these processes. It is seen that the axis of the maximum in precipitation tendency in the CM2.1 simulation (principal signal shaded in green) leads the corresponding feature in the ENSO experiment (contour pattern) by 1–2 pentads (see Fig. 10a), but lags the analogous feature in the IO experiment by 1–2 pentads (see Fig. 10b). This result suggests that the CM2.1 simulation combines the opposing roles of the SST forcings in TPAC and IO in delaying and advancing SASM development, respectively. The net effect, as represented by the CM2.1 data in Fig. 10, is an evolution with timing that is intermediate between that produced individually in the ENSO and IO experiments.

Park et al. (2010) have also examined the trade-off between weakened monsoon circulation after El Niño (which results in dry conditions) and moist processes associated with IO warming (which favors monsoonal rainfall). They further noted that the monsoon circulation is restored during the late monsoon season (August–September), and the sustained IO warming leads to rainfall increases. This development may account for the above-normal *seasonal averaged* monsoon rainfall after major El Niño events.

9. Discussion and conclusions

The air–sea interaction associated with the climatological evolution of the SASM is investigated using long-term averages of the output from a coupled GCM and various observational datasets (Figs. 1–3). It is demonstrated that the monsoonal precipitation is accompanied by changes in the SW and LH fluxes at the underlying ocean surface, and by local oceanic cooling. The resulting pattern of meridional SST gradients facilitates the northward advance of the monsoon rains over South Asia. The leading pair of EEOF modes captures the variability of the timing of this poleward monsoon march in individual years (Fig. 4). Composite analysis of the temporal coefficients of these EEOF modes reveals that SASM development tends to occur earlier than normal in the summers following La Niña development, whereas delayed development is simulated after the mature phase of El Niño events (Figs. 6–8).

The processes contributing to the relationship between SASM development and ENSO are delineated by subjecting the atmospheric component of the coupled GCM to ENSO-related SST forcings in the TPAC and IO basins separately. The sensitivity experiment based on warm SST anomalies in TPAC during El Niño events indicates that this forcing influences the atmospheric circulation over IO through modulation of the strength of the Walker Cell. The anomalous sinking branch of this cell, which is accompanied by suppressed precipitation, migrates to the central equatorial IO during the initiation phase of SASM (Figs. 9a–d). The delay in monsoon development in El Niño episodes may partially be attributed to this geographical and temporal coincidence between the evolution of the atmospheric response to TPAC forcing and SASM development. This effect is opposed by that due to the warm SST anomalies in the IO Basin, which are produced by the atmospheric bridge mechanism during El Niño events. The sensitivity experiment subjected to these SST anomalies in the IO illustrates that the IO warming leads to anomalous large-scale ascent and wet conditions over tropical IO in late May, which tends to accelerate the monsoon evolution process in this region (Figs. 9e–h). The net effect of the competing SST forcings in TPAC and IO, as deduced from the simulation of the coupled GCM, is a monsoon development scenario with a timing that is intermediate between the separate responses to TPAC and IO forcings (Fig. 10).

Although our previous work on the SCS–WNP monsoon (LN09) and the present examination of SASM are based on the same set of model experiments, rather different analysis tools are used in these studies to delineate various features of interest in these two regions. The current investigation also yields new information on the role and relative importance of ENSO-related SST forcings in the TPAC and IO sectors in influencing SASM development. In particular, an EEOF analysis procedure is specifically designed to highlight the migration of precipitation zones both before and after the arrival of the summer monsoon over South Asia. The diagnosis using this approach indicates that remote ENSO forcing from TPAC and local SST anomalies in IO exert comparable but opposing impacts on SASM development (Fig. 9). These findings shed light on the role of different facets of air–sea coupling in the SASM evolution during El Niño events in the CM2.1 experiment. The above results are quite distinct from those obtained for the SCS–WNP monsoon in the LN09 study (see their Fig. 10), which indicates that the monsoon variations in that region during early summer are dominated by responses to remote SST forcings in the TPAC and IO sectors, whereas local SST anomalies in SCS–WNP only play a minor role. In the present study, we have also presented fresh evidence linking ENSO forcing to variability in the northwestward movement of the equatorial convective cloudiness maximum (ECCM) over IO (Fig. 9), which is known to have notable impacts on SASM development. This chain of processes has not been considered in LN09. In summary, our study builds upon the foundation laid by the works of LN09 and many other investigators, and presents some new findings that are of interest to our community.

Goswami and Xavier (2005, see their Fig. 4) have noted that ENSO could influence the atmosphere–ocean conditions in the vicinity of the SASM region by two separate pathways: regulation of the SST in the IO Basin by a tropical atmospheric bridge as described in the beginning of section 7, and modification of the tropospheric temperature (TT) over the Asian landmass near 30°N through dynamical mechanisms. Both of these processes would affect the meridional temperature gradient (ΔTT; see definition in section 4) over South Asia, and hence play a considerable role in the timing of SASM onset. Anomaly charts of TT in early summer have been plotted using composite data for El Niño and La Niña events in the CM2.1 simulation and 30-run averages of the ENSO experiments subjected to El Niño and La Niña forcings. These results (not shown) bear a strong resemblance to their observational counterpart, as presented in Fig. 4a of Goswami and Xavier (2005). In particular, observed and simulated El Niño events are accompanied by increased TT over the IO Basin and decreased TT over the subtropical Asian landmass, which lead to negative anomalies in ΔTT and imply a postponement of monsoon onset. The opposite changes prevail in La Niña episodes. In the present study, we have focused on the relationships between air–sea interactions in the IO Basin and SASM development. In view of the prominent anomalies of the thermal conditions over the subtropical Asian landmass during ENSO, more attention should also be devoted in future studies to the impacts of continental heat sources on monsoon variability over South Asia.

The relationship between ENSO and SASM evolution, as deduced from the model diagnoses, is supported by the observed episodes shown in Figs. 8c,f. However, it should be stressed that only a fraction of the ENSO events in the observational record conform to this relationship. For instance, Joseph et al. (1994, see their Table 9) reported that out of the 31 observed El Niño events during 1870–1989, the monsoon onset over southern India was delayed by more than 8 days in 11 events. These authors also noted that the correlation coefficient between SST anomalies in the central equatorial Pacific and the monsoon onset date is not particularly high (0.32; see their Table 7). The usefulness of the ENSO signal as a predictor of SASM development should be assessed in the context of these statistics.

The focus of this work is the timing of SASM development in early winter and its relationships with local and remote oceanic conditions. Other aspects of this monsoon system that are also of strong interest include intensity of precipitation and circulation at and after onset, timing of the monsoonal withdrawal, total length of the monsoon season, behavior of intraseasonal oscillations within the monsoon season, and interactions between SASM and other flow regimes in neighboring regions. The overall characteristics of the monsoon in a given year (e.g., total rainfall amount, seasonally averaged temperature, number of tropical cyclones, etc.) are dependent not only on the timing of the initiation of monsoon evolution, but also on many of the characteristics listed above. These myriad facets need to be taken into account in future studies of the mean state and variability of the monsoon system.

Acknowledgments. We wish to thank our GFDL colleagues at the Research Group on Climate Change, Variability and Prediction for providing various model datasets and model tools for this study. We are also grateful to Isaac Held, John Lanzante, Bill Stern, Ming Zhao, and the two official reviewers for their insightful comments on earlier versions of this manuscript.

REFERENCES

Alexander, M. A., N.-C. Lau, and J. D. Scott, 2004: Broadening the atmospheric bridge paradigm: ENSO teleconnections to the tropical west Pacific-Indian Oceans over the seasonal cycle and to the North Pacific in summer. *Earth's Climate: The Ocean-Atmosphere Interaction*, *Geophys. Monogr.,* Vol. 147, Amer. Geophys. Union, 85–103.

Bellon, G., and A. Sobel, 2008: Poleward-propagating intraseasonal monsoon disturbances in an intermediate-complexity axisymmetric model. *J. Atmos. Sci.,* **65,** 470–489.

Chang, C.-P., P. Harr, and J. Ju, 2001: Possible roles of Atlantic circulations on the weakening Indian monsoon rainfall–ENSO relationship. *J. Climate,* **14,** 2376–2380.

Delworth, T. L., and Coauthors, 2006: GFDL's CM2 global coupled climate models. Part I: Formulation and simulation characteristics. *J. Climate,* **19,** 643–674.

Ding, Y., and D. R. Sikka, 2006: Synoptic systems and weather. *The Asian Monsoon,* B. Wang, Ed., Springer, 131–201.

Fu, X., B. Wang, T. Li, and J. P. McCreary, 2003: Coupling between northward-propagating, intraseasonal oscillations and sea surface temperature in the Indian Ocean. *J. Atmos. Sci.,* **60,** 1733–1753.

——, ——, D. E. Waliser, and L. Tao, 2007: Impact of atmosphere–ocean coupling on the predictability of monsoon intraseasonal oscillations. *J. Atmos. Sci.,* **64,** 157–174.

Gadgil, S., M. Rajeevan, L. Zubair, and P. Yadav, 2011: South Asian monsoon: Interannual variation. *The Global Monsoon System: Research and Forecast,* 2nd ed., C.-P. Chang, Ed., World Scientific, 25–42.

GFDL Global Atmospheric Model Development Team, 2004: The new GFDL global atmosphere and land model AM2–LM2: Evaluation with prescribed SST simulations. *J. Climate,* **17,** 4641–4673.

Goswami, B. N., 2005a: South Asian monsoon. *Intraseasonal Variability in the Atmosphere-Ocean Climate System,* W. K. M. Lau and D. E. Waliser, Eds., Springer, 19–61.

——, 2005b: South Asian summer monsoon: An overview. The global monsoon system: Research and forecast, World Meteorological Organization Tech. Rep. WMO/TD 1266, 47–71.

——, and P. K. Xavier, 2005: ENSO control on the south Asian monsoon through the length of the rainy season. *Geophys. Res. Lett.,* **32,** L18717, doi:10.1029/2005GL023216.

Griffies, S. M., M. J. Harrison, R. C. Pacanowski, and A. Rosati, 2003: A technical guide to MOM4. NOAA/GFDL Ocean Group Tech. Rep. 5, 295 pp.

Jiang, X., T. Li, and B. Wang, 2004: Structures and mechanisms of the northward propagating boreal summer intraseasonal oscillation. *J. Climate,* **17,** 1022–1039.

Joseph, P. V., J. K. Eischeid, and R. J. Pyle, 1994: Interannual variability of the onset of the Indian summer monsoon and its association with atmospheric features, El Niño, and sea surface temperature anomalies. *J. Climate,* **7,** 81–105.

——, K. P. Sooraj, and C. K. Rajan, 2006: The summer monsoon onset process over South Asia and an objective method for the date of monsoon onset over Kerela. *Int. J. Climatol.,* **26,** 1871–1893.

Kang, I.-S., C.-H. Ho, Y.-K. Lim, and K.-M. Lau, 1999: Principal modes of climatological seasonal and intraseasonal variations of the Asian summer monsoon. *Mon. Wea. Rev.,* **127,** 322–340.

Klein, S. A., B. J. Soden, and N.-C. Lau, 1999: Remote sea surface temperature variations during ENSO: Evidence for a tropical atmospheric bridge. *J. Climate,* **12,** 917–932.

Krishnamurti, T. N., and N. Surgi, 1987: Observational aspects of summer monsoon. *Monsoon Meteorology, Oxford Monogr. Geol. Geophys.,* No. 7, Oxford University Press, 3–25.

Kug, J.-S., J. Choi, S.-I. An, F.-F. Jin, and A. T. Wittenberg, 2010: Warm pool and cold tongue El Niño events as simulated by the GFDL 2.1 coupled GCM. *J. Climate,* **23,** 1226–1239.

Larkin, N. K., and D. E. Harrison, 2002: ENSO warm (El Niño) and cold (La Niña) event life cycles: Ocean surface anomaly patterns, their symmetries, asymmetries, and implications. *J. Climate,* **15,** 1118–1140.

Lau, N.-C., and M.-J. Nath, 2003: Atmosphere–ocean variations in the Indo-Pacific sector during ENSO episodes. *J. Climate,* **16,** 3–20.

——, and ——, 2009: A model investigation of the role of air–sea interaction in the climatological evolution and ENSO-related variability of the summer monsoon over the South China Sea and western North Pacific. *J. Climate,* **22,** 4771–4792.

Li, C., and M. Yanai, 1996: The onset and interannual variability of the Asian summer monsoon in relation to land–sea thermal contrast. *J. Climate,* **9,** 358–375.

Park, H.-S., J. C. H. Chiang, B. R. Lintner, and G. J. Zhang, 2010: The delayed effect of major El Niño events on Indian monsoon rainfall. *J. Climate,* **23,** 932–946.

Pegion, K., and B. P. Kirtman, 2008: The impact of air–sea interactions on the simulation of tropical intraseasonal variability. *J. Climate,* **21,** 6616–6635.

Rajendran, K., and A. Kitoh, 2006: Modulation of tropical intraseasonal oscillations by ocean–atmosphere coupling. *J. Climate,* **19,** 366–391.

Robock, A., M. Mu, K. Vinnikov, and D. Robinson, 2003: Land surface conditions over Eurasia and Indian summer monsoon rainfall. *J. Geophys. Res.,* **108,** 4131, doi:10.1029/2002JD002286.

Sengupta, D., and M. Ravichandran, 2001: Oscillations of Bay of Bengal sea surface temperature during the 1998 summer monsoon. *Geophys. Res. Lett.,* **28,** 2033–2036.

——, B. N. Goswami, and R. Senan, 2001: Coherent intraseasonal oscillations of ocean and atmosphere during the Asian Summer Monsoon. *Geophys. Res. Lett.,* **28,** 4127–4130.

Shukla, J., 1987: Interannual variability of monsoons. *Monsoons,* J. S. Fein and P. L. Stephens, Eds., Wiley-Interscience, 399–463.

Wang, B., and X. Xu, 1997: Northern Hemisphere summer monsoon singularities and climatological intraseasonal oscillation. *J. Climate,* **10,** 1071–1085.

——, and H. Lin, 2002: Rainy season of the Asian-Pacific summer monsoon. *J. Climate,* **15,** 386–396.

——, Q. Ding, and P. V. Joseph, 2009: Objective definition of the Indian summer monsoon onset. *J. Climate,* **22,** 3303–3316.

Weare, B. C., and J. S. Nasstrom, 1982: Examples of extended empirical orthogonal function analyses. *Mon. Wea. Rev.,* **110,** 481–485.

Webster, P. J., 1983: Mechanisms of monsoon low-frequency variability: Surface hydrological effects. *J. Atmos. Sci.,* **40,** 2110–2124.

——, 2006: The coupled monsoon system. *The Asian Monsoon,* B. Wang, Ed., Springer, 3–66.

——, V. O. Magaña, T. N. Palmer, J. Shukla, R. A. Tomas, M. Yanai, and T. Yasunari, 1998: Monsoons: Processes, predictability, and the prospects for projection. *J. Geophys. Res.,* **103,** 14 451–14 510.

Xie, S.-P., K. Hu, J. Hafner, H. Tokinaga, Y. Du, G. Huang, and T. Sampe, 2009: Indian Ocean capacitor effect on Indo–western Pacific climate during the summer following El Niño. *J. Climate,* **22,** 730–747.

Yanai, M., C. Li, and Z. Song, 1992: Seasonal heating of the Tibetan Plateau and its effects on the evolution of the Asian summer monsoon. *J. Meteor. Soc. Japan,* **70,** 319–351.

Yang, S., K. M. Lau, and M. S. Rao, 1996: Precursory signals associated with the interannual variability of the Asian summer monsoon. *J. Climate,* **9,** 949–964.